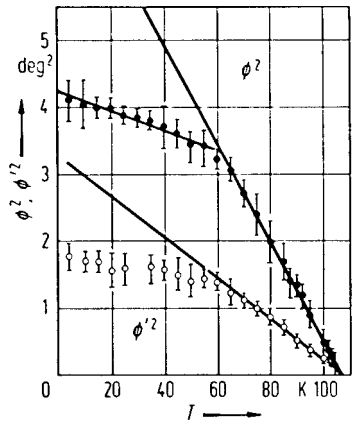

Fig. 1A-8-120. $SrTiO_3$. ϕ^2, ϕ'^2 vs. T [70Uno1]. ϕ and ϕ' are the rotation angles of oxygen octahedra observed by ESR of Fe^{3+} ions at Ti-site without and with nearest-neighbour oxygen vacancy, respectively.

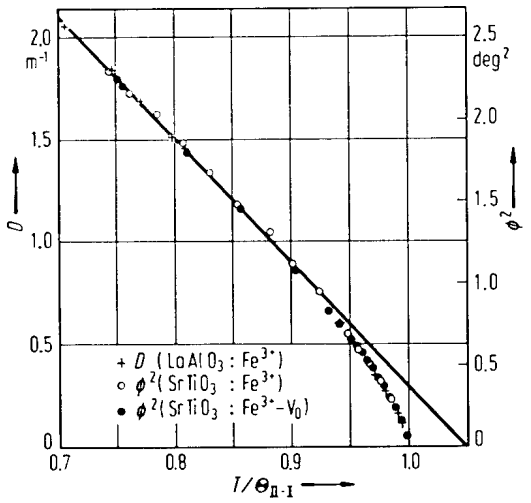

Fig. 1A-8-121. $SrTiO_3$, $LaAlO_3$. ϕ^2 ($SrTiO_3$), D ($LaAlO_3$) vs. T/Θ_{II-I} [71Mor]. ϕ: rotation angle of oxygen octahedron, D: axial spin Hamiltonian parameter for Fe^{3+} ion. V_O means oxygen vacancy. See also **Fig**. 1A-8-120.

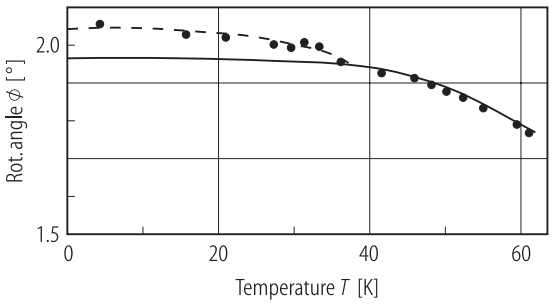

Fig. 1A-8-122. $SrTiO_3$:Fe^{3+}. ϕ vs. T [71Mul]. ϕ: rotation angle of octahedra determined by EPR measurement for $H \parallel [100] - 32^o$ in a (001) plane. Full curve: calculated. See [91Mul].

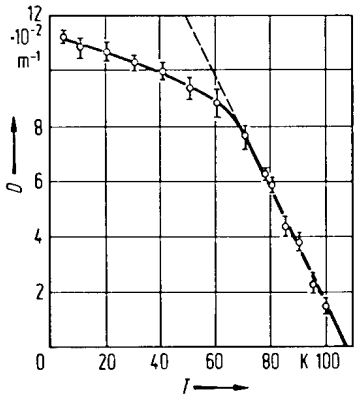

Fig. 1A-8-123. $SrTiO_3$. *D* vs. *T* [70Uno1]. *D*: axial spin Hamiltonian parameter for Fe^{3+} ion.

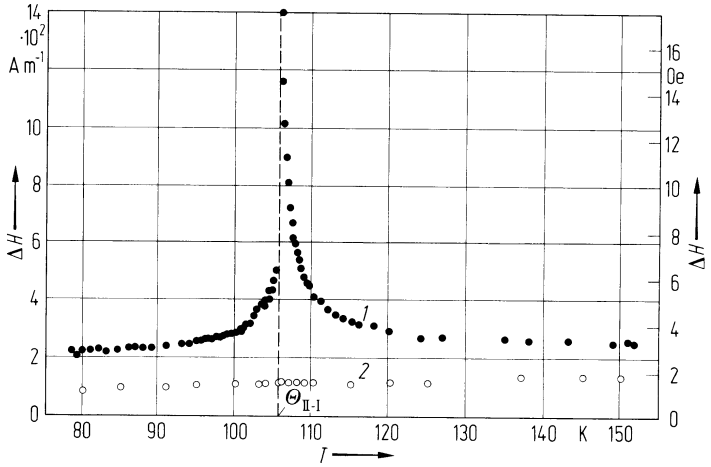

Fig. 1A-8-124. $SrTiO_3$. ΔH vs. T [72von1]. ΔH: ESR line width due to Fe^{3+}–V_O center at 19.2 GHz, where Fe^{3+}–V_O means Fe^{3+} with a nearest-neighbour oxygen vacancy. Curve *1*: high-field line, *2*: low-field line ($g \approx 6$).

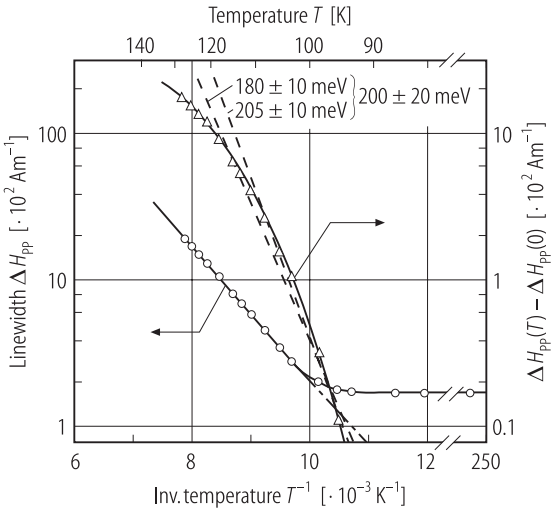

Fig. 1A-8-125. $SrTiO_3$:V^{2+}. ΔH_{pp} vs. 1/ T [90Mul]. ΔH_{pp}: peak to peak linewidth of V^{2+} hyperfine line. Open circles: ΔH_{pp}, open triangles: $\Delta H_{pp}(T) - \Delta H_{pp}(0)$.

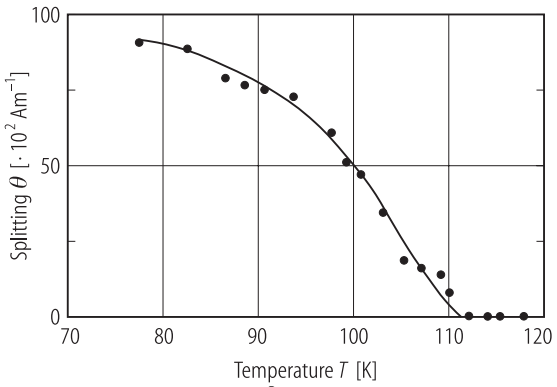

Fig. 1A-8-126. $SrTiO_3$:Fe^{3+}. θ vs. T [67Uno]. θ: splitting of strong field linewidth with H_{ex} at 15° away from <100>.

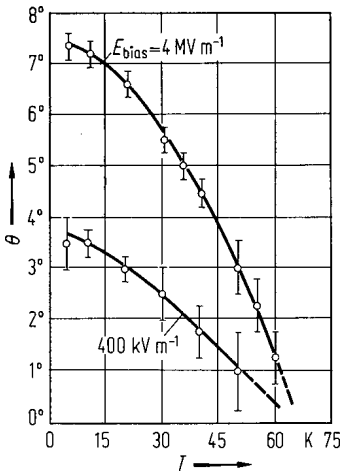

Fig. 1A-8-127. $SrTiO_3$. θ vs. T [70Uno2]. Parameter: E_{bias}.
θ: splitting angle of ESR spectrum due to Gd^{3+}.

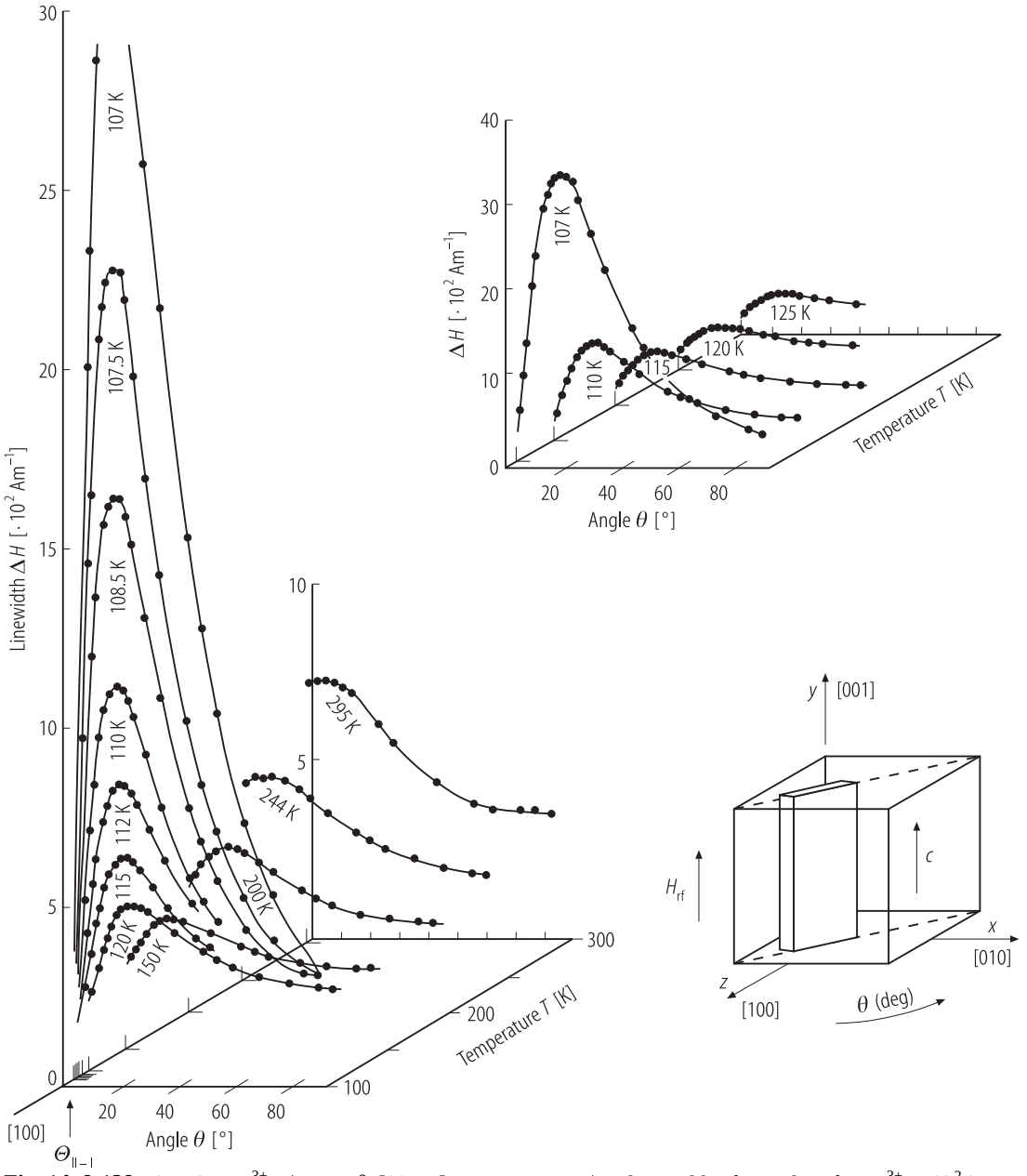

Fig. 1A-8-128. $SrTiO_3$: Fe^{3+}. ΔH vs. θ [80Rei]. Parameter: T. ΔH: linewidth of EPR line for Fe^{3+}–$V(O^{2-})$ center, θ: rotation angle. Insert shows a sample geometry, where the magnetic field was rotated in z–x plane.

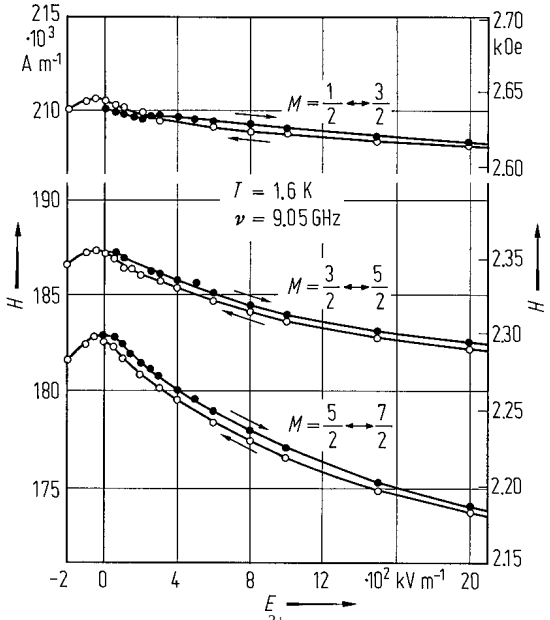

Fig. 1A-8-129. $SrTiO_3 : Gd^{3+}$. *H* vs. *E* [66Sak]. Parameter: *M*. *M*: magnetic quantum number. *H* || [100], *E* || [100].

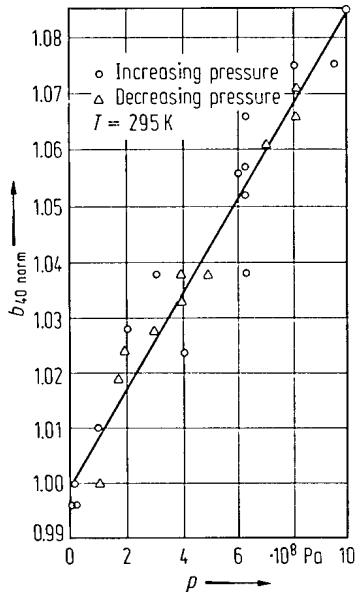

Fig. 1A-8-130. $SrTiO_3$: Fe^{3+}. $b_{40\ norm}$ vs. p [64Rim]. $b_{40\ norm} = b_{40}(p) / b_{40}(p = 0)$. b_{40} is defined by Eq. (8) of Table IC-4 in Introduction.

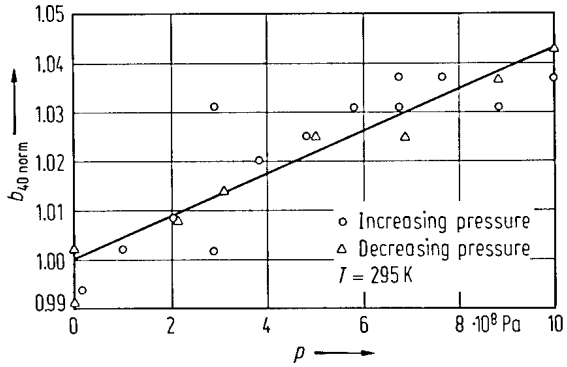

Fig. 1A-8-131. $SrTiO_3 : Gd^{3+}$. $b_{40\ norm}$ vs. p [64Rim]. $b_{40\ norm} = b_{40}(p) / b_{40}(p = 0)$. b_{40} is defined by Eq. (8) of Table IC-4 in Introduction.

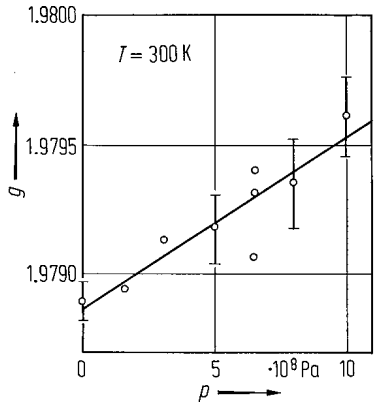

Fig. 1A-8-132. $SrTiO_3 : Cr^{3+}$. g vs. p [64Rim]. Cr^{3+} in cubic site.

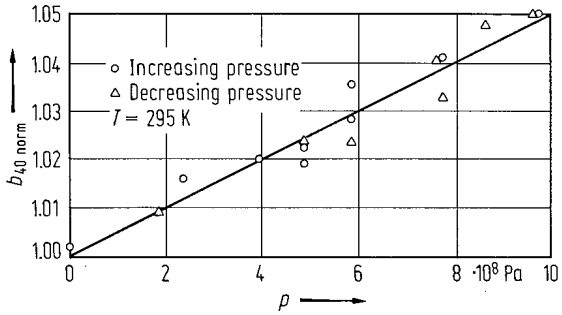

Fig. 1A-8-133. $SrTiO_3 : Eu^{2+}$. $b_{40\ norm}$ vs. p [64Rim]. $b_{40\ norm} = b_{40}(p) / b_{40}(p = 0)$. b_{40} is defined by Eq. (8) of Table IC-4 in Introduction.

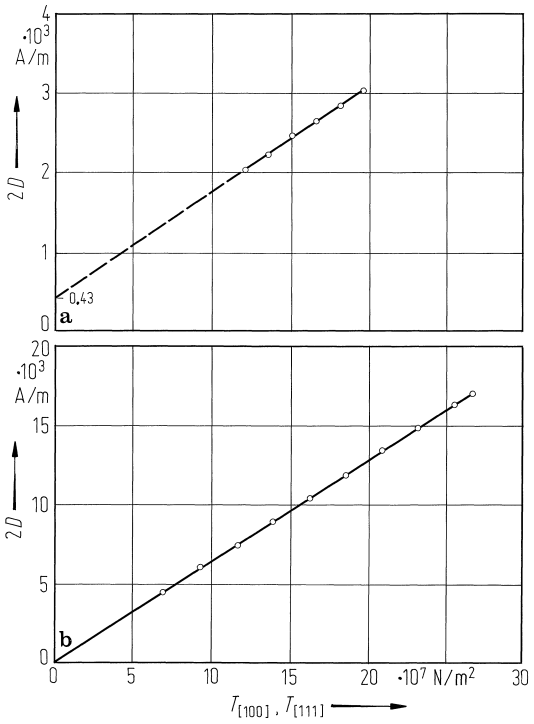

Fig. 1A-8-134. $SrTiO_3$. $2D$ vs. $T_{[hkl]}$ [83Mul]. Parameter: T. D: FS parameter for Cr^{3+} center, $T_{[hkl]}$: uniaxial stress. **(a)** [100] direction, **(b)** [111] direction.

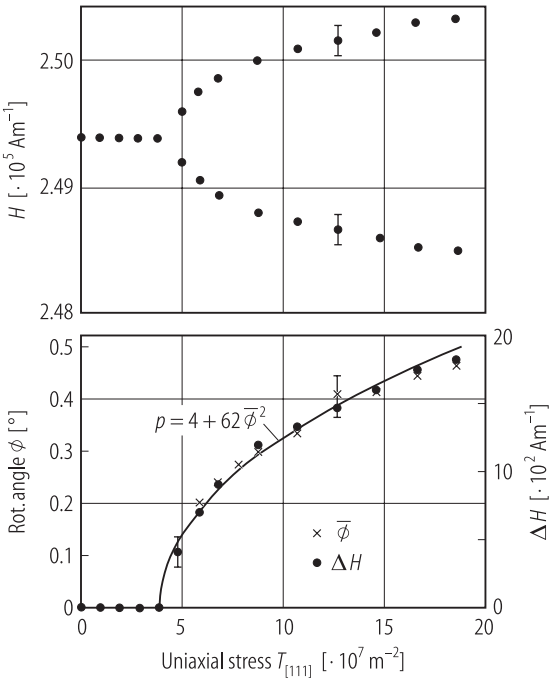

Fig. 1A-8-135. $SrTiO_3 : Fe^{3+}$. H, ΔH, ϕ vs. $T_{[111]}$ [70Mul]. H: magnetic field of EPR spectral line ($H \parallel [1\bar{1}0]$), ΔH: splitting of EPR lines resulting from Fe^{3+}–$V(O^{2-})$ centers, ϕ: rotation angle, $T_{[111]}$: uniaxial stress in [111] direction. T = 104 K.

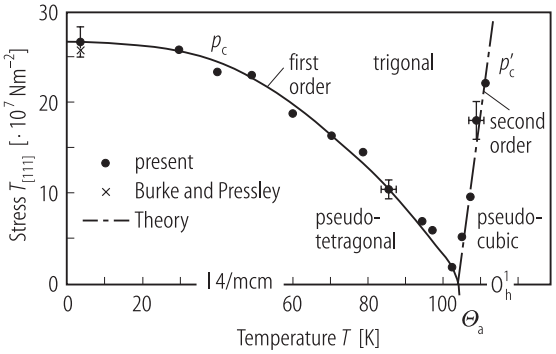

Fig. 1A-8-136. $SrTiO_3$: Fe^{3+}. $T_{[111]}$ $-T$ phase diagram [70Mul]. Stress-induced trigonal phase $R\bar{3}c$. Full circles: [70Mul], crosses: [69Bur]. Θ_a = 103.0(1) K (a little lower than those published in literature; see note in [70Mul]).

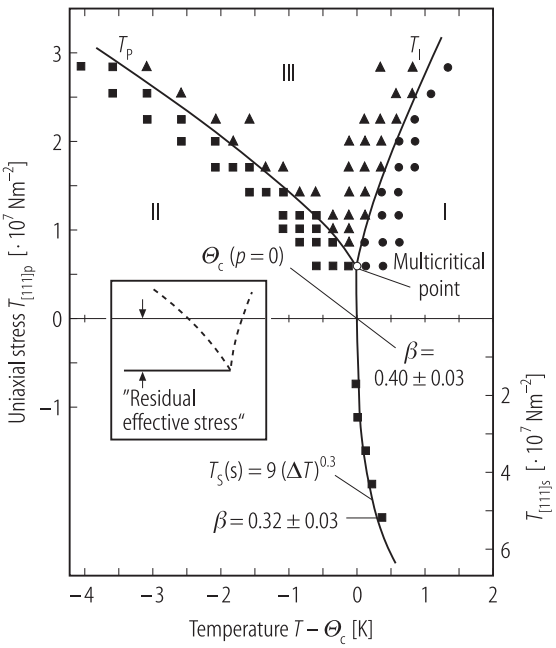

Fig. 1A-8-137. $SrTiO_3$. $T_{[111]} - T$ phase diagram [82Mul]. $T_{[111]p}$, $T_{[111]s}$: uniaxial stress in [111] direction, compressional (p) and stretching (s). I: pseudocubic, II: pseudotetragonal, III: trigonal, $R\bar{3}c$. Phase boundaries were determined under compressional and extensional stress, using EPR with $H \parallel [110]$. Insert is a magnified diagram in the vicinity of Θ_c. β's indicate values of order parameter exponent under tension.

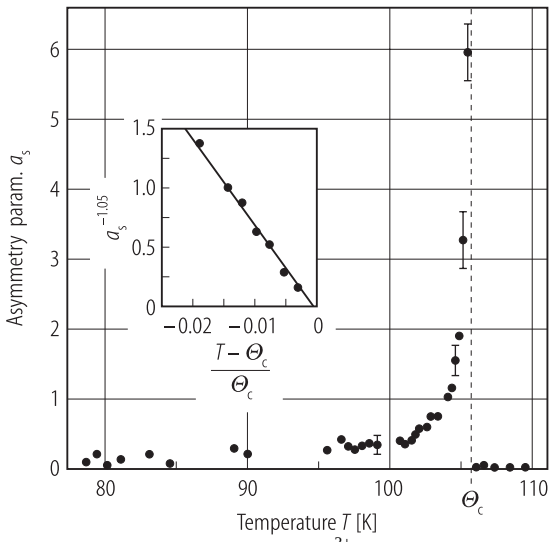

Fig. 1A-8-138. $SrTiO_3$: Fe^{3+}. a_s vs. T [72Mul]. a_s: asymmetry parameter in EPR spectrum due to Fe^{3+}–$V(O^{2-})$ pair centers. Solid curve in the insert is calculated with $a_s = a_0 (\Theta_c - T)^{-1.05}$.

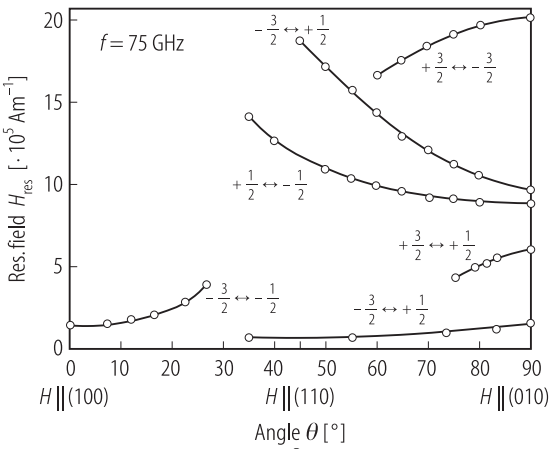

Fig. 1A-8-139. $SrTiO_3$: Fe^{3+}. H_{res} vs. θ [68Bae]. H_{res}: resonance field in EPR of Fe^{3+}, θ: angle of crystal orientation. Specimen was cut parallel to (001) plane and the magnetic field was applied perpendicular to (001) plane. f = 75 GHz, T = RT.

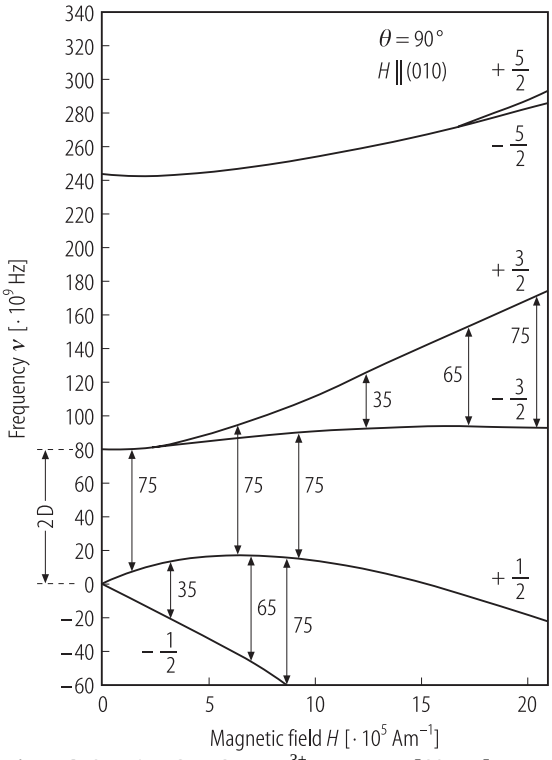

Fig. 1A-8-140. $SrTiO_3$: Fe^{3+}. ν vs. H [68Bae]. Energy level diagram. ν: frequency (for energy scale), H: magnetic field strength for θ = 90°. The energy of M_s = ±1/2 doublet is chosen arbitrarily to be zero in zero field. Vertical arrows mark the transitions which may be observed at 35, 65 and 75 GHz.

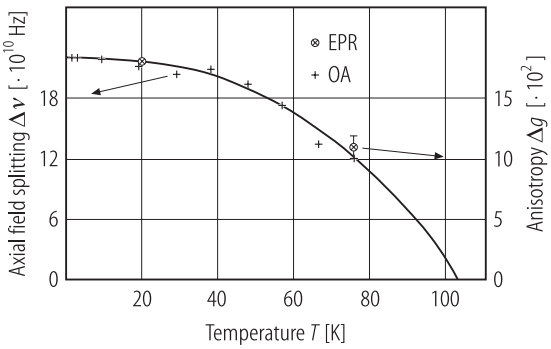

Fig. 1A-8-141. $SrTiO_3$: Ir^{4+}. $\Delta\nu$, Δg vs. T [84Shi]. $\Delta\nu$: axial field splitting measured by infrared optical absorption, Δg: axial anisotropy of g values ($\Delta g = g_\perp - g_\parallel$) determined by EPR. Solid curve shows tetragonality against T [68Mul].

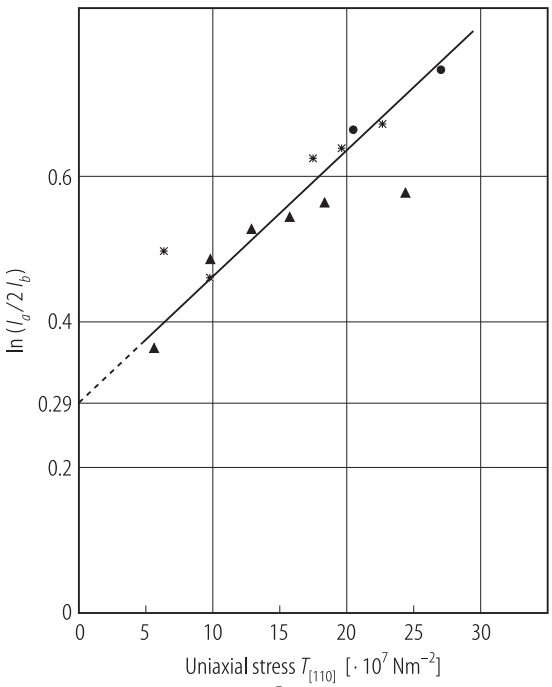

Fig. 1A-8-142. $SrTiO_3 : Cr^{5+}$. $\ln(I_a / 2I_b)$ vs. $T_{[110]}$ [76deJ]. I_a / I_b: peak intensity ratio of EPR line derivatives. Resonance spectrum line **(**a**)** stems from Cr^{5+} ions in a [100] domain, whereas line **(**b**)** originates from centers present in all domains, which have their tetragonal axes along [001] above Θ_{II-I}. $T_{[110]}$: uniaxial stress in [110] direction. $H \parallel [001]$. $T = 77$ K.

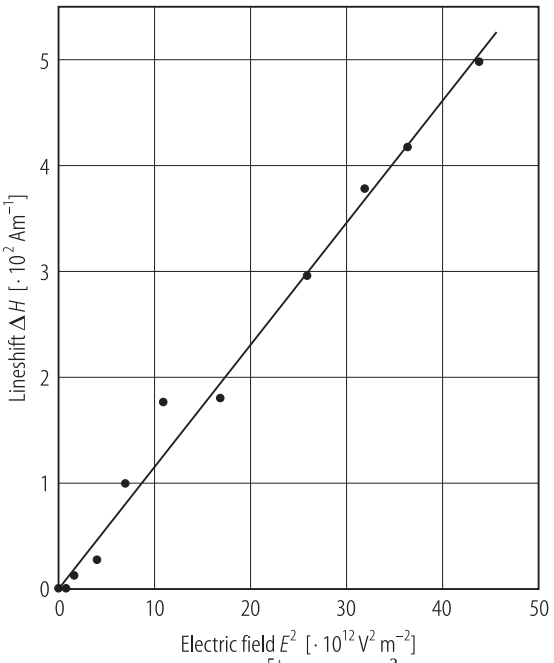

Fig. 1A-8-143. $SrTiO_3 : Cr^{5+}$. ΔH vs. E^2 [78deJ]. ΔH: shift of line y in EPR spectra, E: electric field applied in [001] direction with $H \parallel$ [100]. Line y is designated for the spectrum due to t-Cr^{5+} center with tetragonal axis making an angle of about 55^o with H.

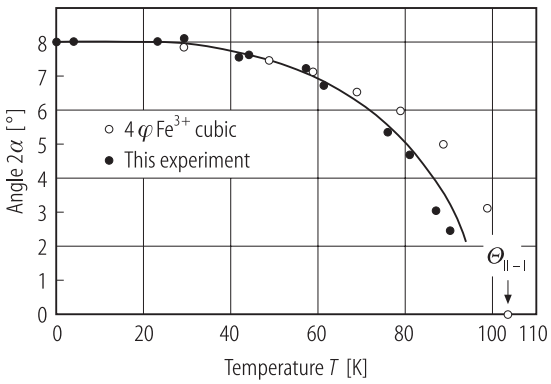

Fig. 1A-8-144. $SrTiO_3 : Cr^{5+}$. 2α, 4ϕ vs. T [93Mul]. α: orthorhombic Cr^{5+} rotation angle determined by EPR, ϕ: rotation angle of octahedra determined for cubic Fe^{3+}. Full circles: 2α, open circles: 4ϕ (Fe^{3+} values have been normalized to that of Cr^{5+} at $T = 0$ K).

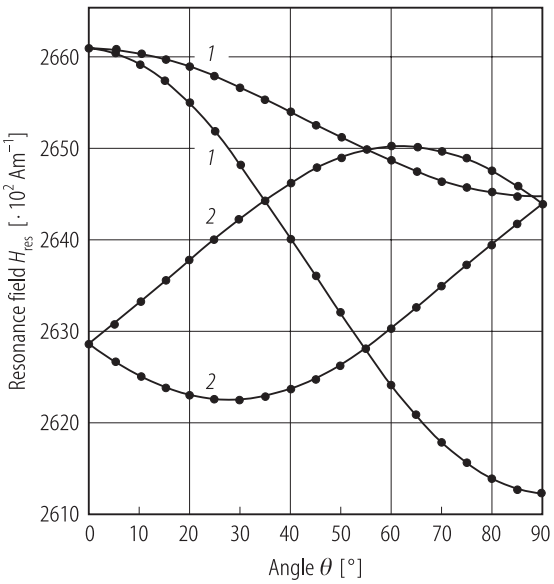

Fig. 1A-8-145. $SrTiO_3 : Cr^{5+}$. H_{res} vs. θ [94Koo]. H_{res}: EPR lines for orthorhombic Cr^{5+} with H in (110) plane and f = 9.1 GHz, θ: rotation angle from [001] axis. Curves represent computer-simulated fits.

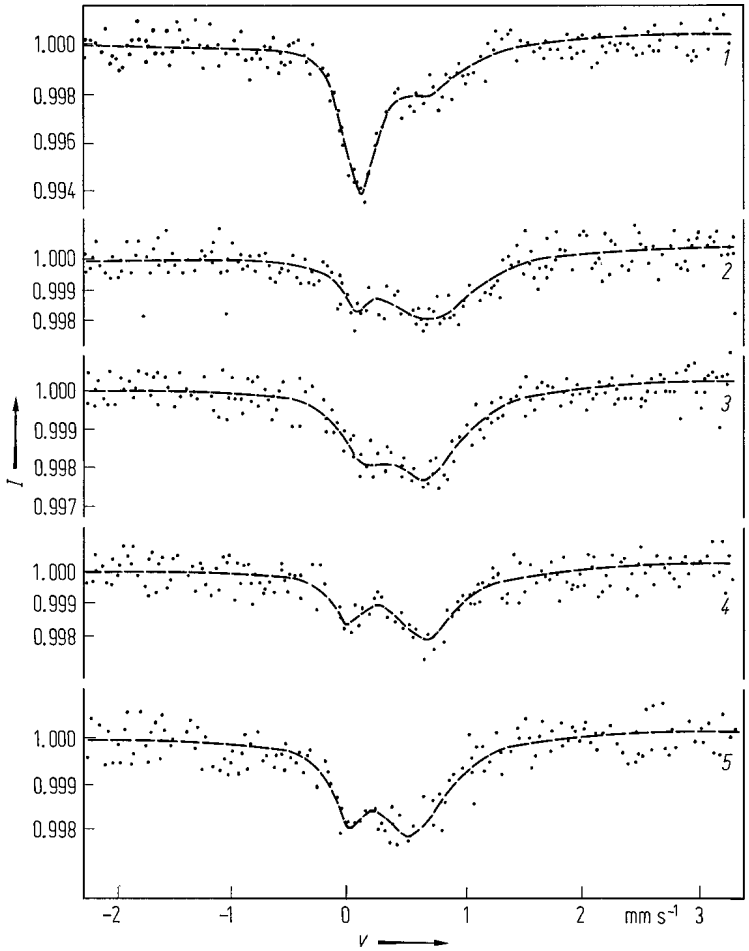

Fig. 1A-8-146. $SrTiO_3$: ^{57}Fe. Mössbauer spectra [73Lui]. *v*: source velocity, I: counting rate (arbitrary units). Curve *1*: Fe-doped $SrTiO_3$, *2*: Fe-doped $SrTiO_3$ after reducing for ½ h, *3*: Fe-doped $SrTiO_3$ after reducing for 4 h, *4*: Fe-doped $SrTiO_3$ after reducing for 36 h, *5*: Fe/Mo-doped $SrTiO_3$.

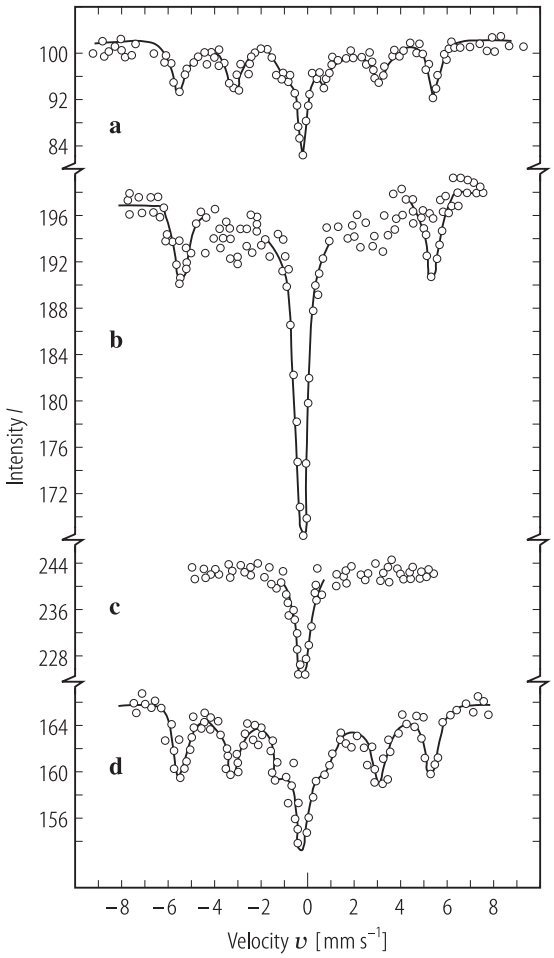

Fig. 1A-8-147. $SrTiO_3$. *I* vs. υ [68Bhi]. Mössbauer spectra for ^{57}Fe. *I*: count rate, υ: source velocity. Parameter: concentration of doped Fe (in atomic %); (**a**) 3.0 %, (**b**) 1.5 %, (**c**) 0.3 %, (**d**) 3 %. Temperature: (**a**, **b**, **c**) RT, (**d**) 78 K. Samples were fired in hydrogen atmosphere at 1000 °C for 2 h.

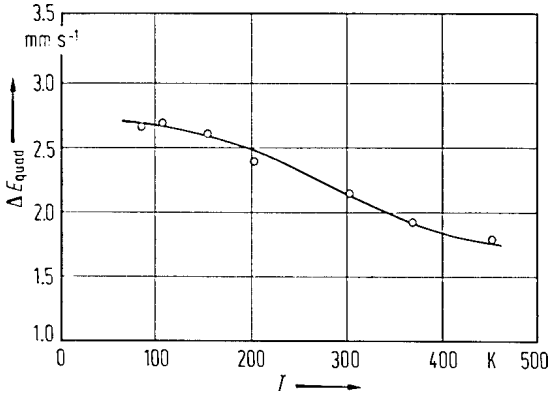

Fig. 1A-8-148. $SrTiO_3$: ^{57}Co (air-quenched). ΔE_{quad} vs. T [67Bhi]. ΔE_{quad}: Fe^{2+}-site quadrupole splitting.

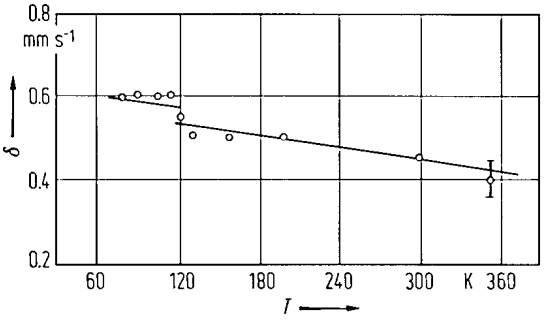

Fig. 1A-8-149. $SrTiO_3$: ^{57}Co (air-quenched). δ vs. T [67Bhi]. δ: isomer shift for Fe^{3+} state.

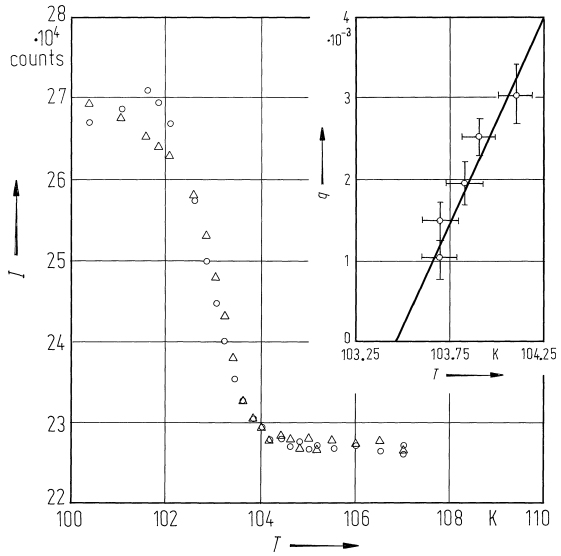

Fig. 1A-8-150. $SrTiO_3$. *I* vs. *T* [86And]. *I*: X-ray diffraction intensity of (113) Bragg reflection. Open triangles: on cooling, open circles: on warming with a rate of about 1 K/ h. Insert: *q* vs. *T*. *T*: temperature corresponding to maximum intensity of diffuse scattering at (0.5 + *q*, 0.5 + *q*, 2.5) on cooling. Extrapolation of transition temperatures indicates 103.45(10) K at $q \rightarrow 0$.

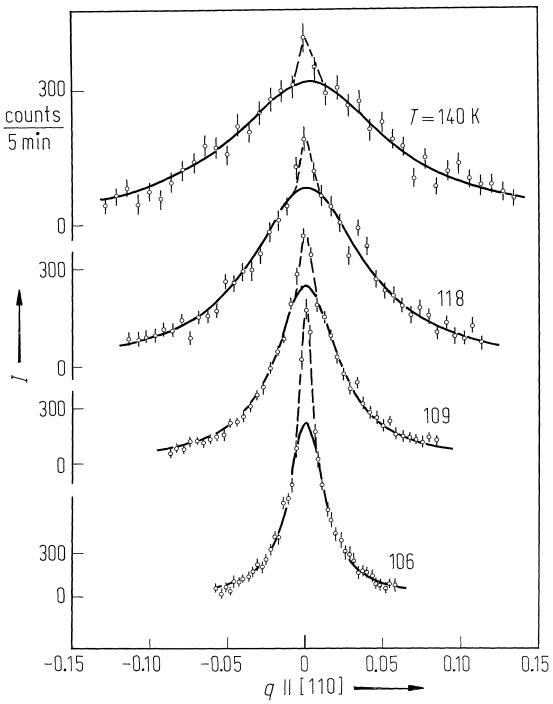

Fig. 1A-8-151. $SrTiO_3$. I vs. q [86And]. Parameter: T ($> \Theta_{II-I}$ = 103.65 K). I: X-ray diffuse scattering intensity along [110] through (0.5, 0.5, 2.5). Curves are least square fit to a model scattering function convoluted with instrumental resolution function. Wave vector width of the broken curve component is limited by instrumental resolution.

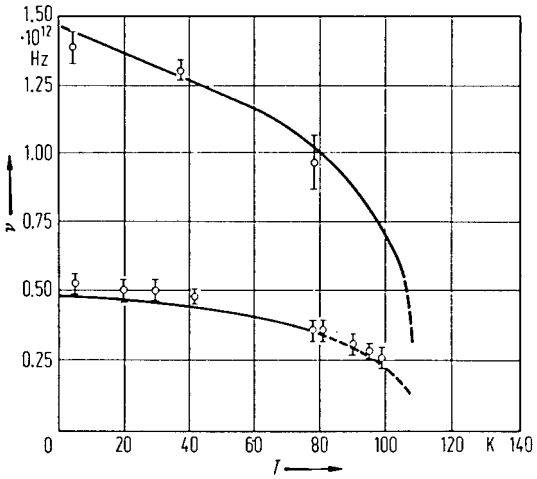

Fig. 1A-8-152. $SrTiO_3$. ν vs. T [69Shi]. ν: phonon frequency at R-point (1.5, 1.5, 2.5) in reciprocal space.

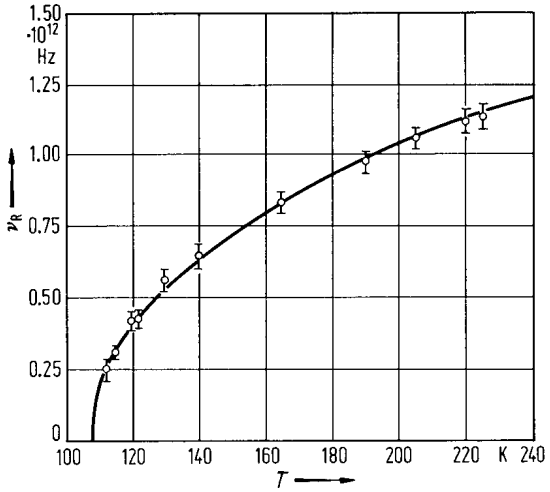

Fig. 1A-8-153. $SrTiO_3$. ν_R vs. T [69Shi]. ν_R: frequency of R_{25} (Γ_{25}) optical phonon.

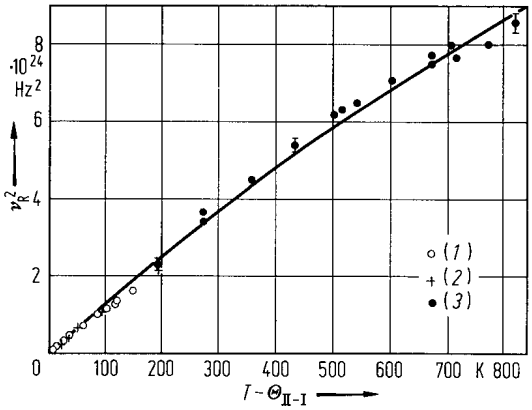

Fig. 1A-8-154. $SrTiO_3$. ν_R^2 vs. $T-\Theta_{II-I}$ [69Shi]. ν_R: frequency of R_{25} (Γ_{25}) optical phonon. (*1*): [69Shi], (*2*): [69Cow], (*3*): [71Otn].

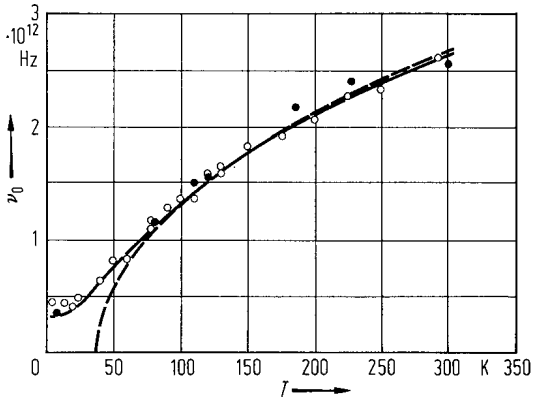

Fig. 1A-8-155. $SrTiO_3$. ν_0 vs. T [69Yam]. ν_0: frequency of soft phonon at $q = 0$. Open circles: inelastic neutron scattering [69Yam], full circles: Raman scattering [67Wor]. Solid curve: $194.4 \cdot \kappa^{-1/2}$; dashed curve: $0.677(T - T_0)^{1/2}$. κ: dielectric constant. $T_0 = 38$ K.

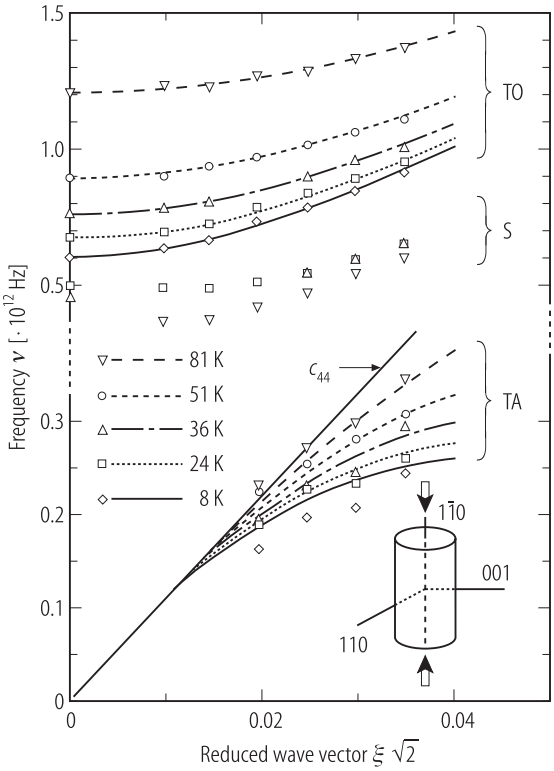

Fig. 1A-8-156. $SrTiO_3$. ν vs. $\xi\sqrt{2}$ [93Mul]. Parameter: T. ν: frequency of phonon, ξ: reduced wave vector for phonon with wave vector $\boldsymbol{Q}$ = (ξ, ξ, 2). Three branches are labelled TO for $A_{2u}(z)$ mode, S for E_g structural mode and TA for acoustic phonon mode related to c_{44}. A straight line marked c_{44} stands for extrapolation from phonon velocity in Brillouin scattering region. Uniaxial pressure of $1.19 \cdot 10^7$ N m^{-2} is applied in $[1\bar{1}0]$ direction.

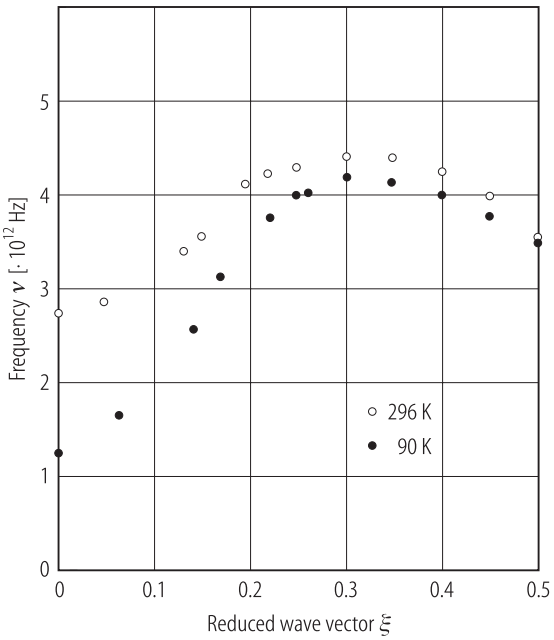

Fig. 1A-8-157. $SrTiO_3$. ν vs. ξ [62Cow]. Dispersion curve of the lowest TO branch along [100]. Parameter: *T*. ν: frequency of phonon, ξ: reduced wave vector.

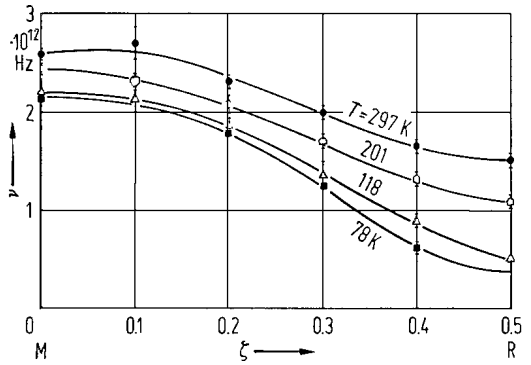

Fig. 1A-8-158. $SrTiO_3$. ν vs. ζ [72Sti]. Parameter: T. ν: phonon frequency, ζ: reduced wave vector coordinate along [1/2, 1/2, ζ].

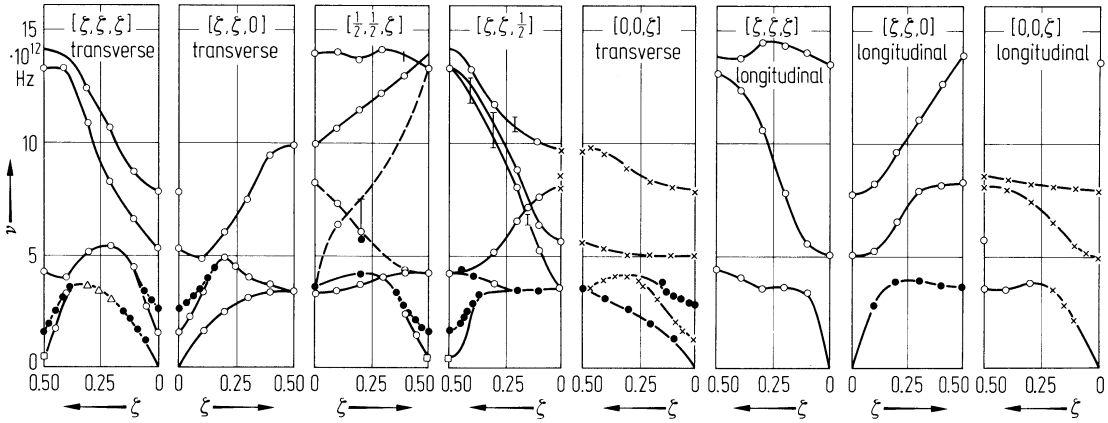

Fig. 1A-8-159. $SrTiO_3$. ν vs. ζ [72Sti]. Parameter: T. ν: frequency of transverse or longitudinal phonon, ζ: reduced wave vector coordinate in various directions indicated in the respective **fig**ures. Open circles: T = 90 K, full circles: T = 297 K [72Sti]; crosses: T = 90 K [64Cow]; squares: T = 120 K [69Shi].

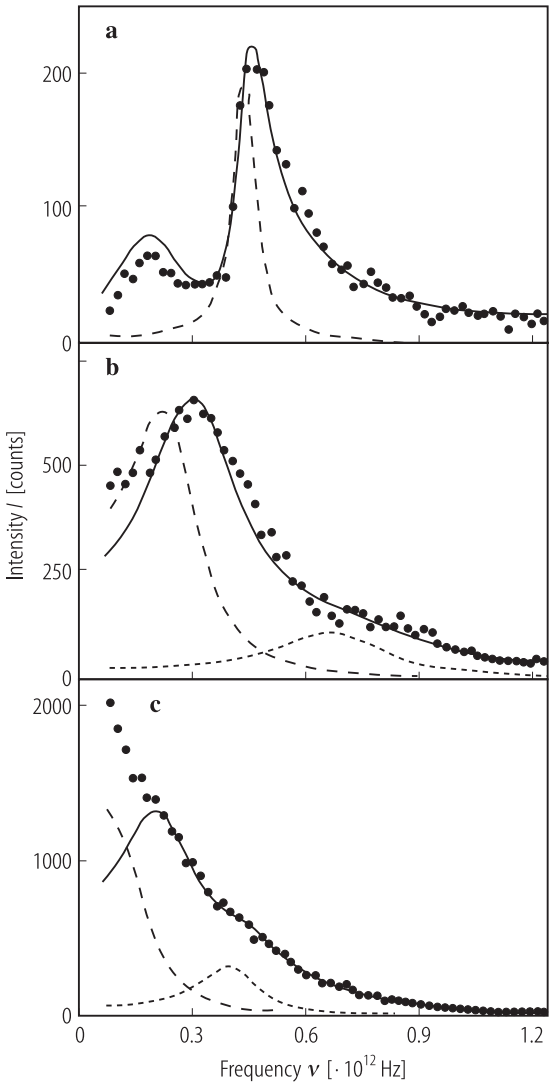

Fig. 1A-8-160. $SrTiO_3$. I vs. ν [83Bru]. I: neutron scattering intensity at R-point. T: (**a**) 15.2 K, (**b**) 86.5 K, (**c**) 98.5 K. Solid curves show the resolution-corrected spectral function obtained from least-square fitting. Long and short broken curves show the actual soft-mode spectral functions without resolution broadening for E_g and A_{1g} phonons with arbitrary normalization, respectively.

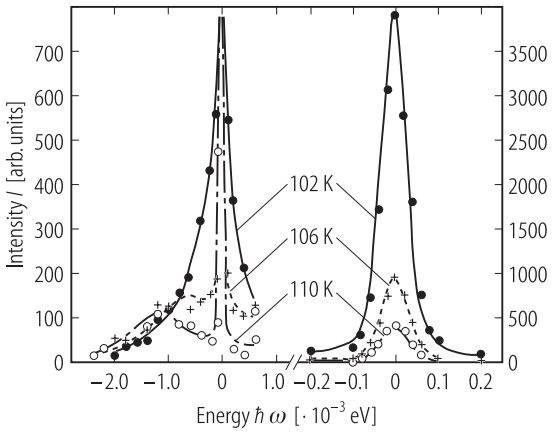

Fig. 1A-8-161. $SrTiO_3$. I vs. $\hbar\omega$ [72Sha]. Parameter: T. I: scattered neutron intensity (in arbitrary scale) for Γ_{25} phonon with wave vector $\boldsymbol{Q}$ = (1/2, 1/2, 3/2). E_0 = 4.9 meV, Θ_{II-I} = 99.5(3) K. The left-hand side shows soft mode behavior of the phonon, whereas the right-hand side shows divergence of the central peak.

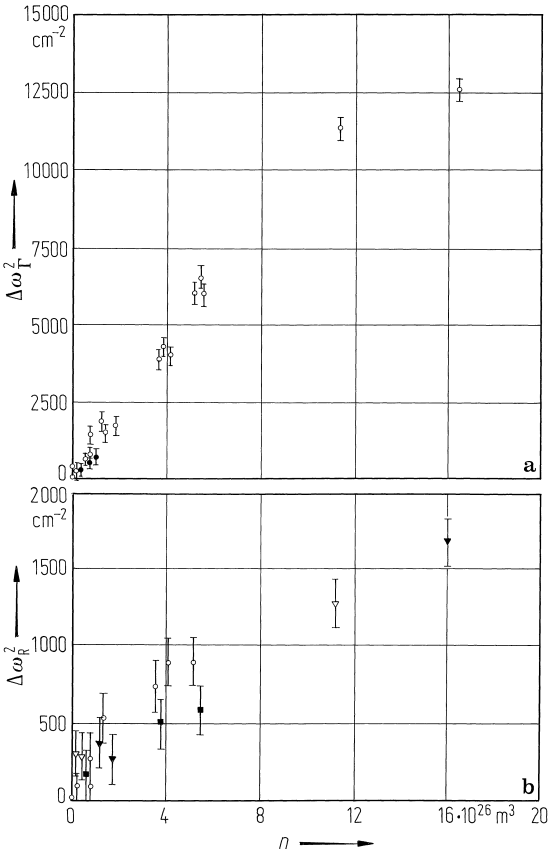

Fig. 1A-8-162. $SrTiO_3$ (reduced). $\Delta\omega^2$ vs. n [80Wag]. $\Delta\omega^2 = \omega^2(\boldsymbol{q}, T, n) - \omega^2(\boldsymbol{q}, T, 0)$. ω : soft mode frequency, n: oxygen vacancy concentration. Subscripts Γ and R refer the zone center and the zone boundary, respectively. (**a**) open circles: neutron data at 300 K, full circles: Raman data at 130 K; (**b**) different symbols correspond to different samples.

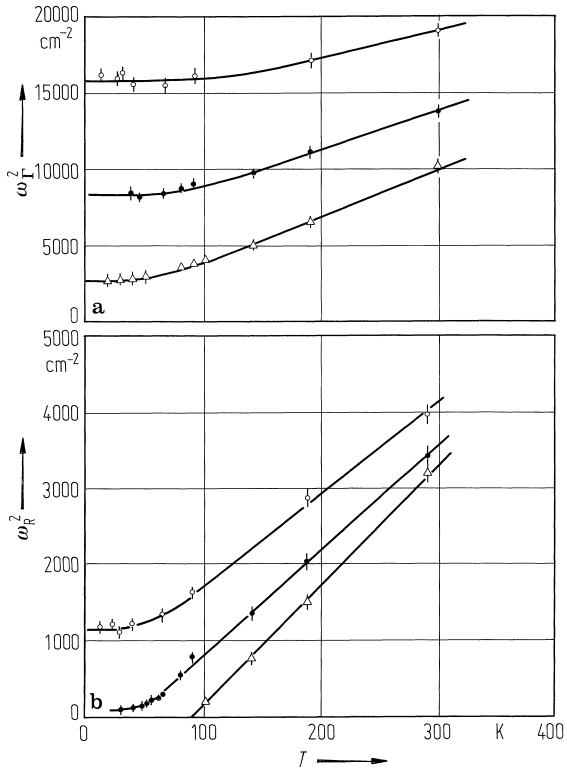

Fig. 1A-8-163. $SrTiO_3$ (reduced). ω^2 vs. T [80Wag]. Parameter: n. ω^2: soft mode frequency squared. Subscripts Γ and R refer to zone center and zone boundary, respectively. n: oxygen vacancy concentration. Open triangles: $n = 1.18 \cdot 10^{26}$ m^{-3}, full circles: $n = 5.32 \cdot 10^{26}$ m^{-3}, open circles: $n = 1.12 \cdot 10^{26}$ m^{-3}.

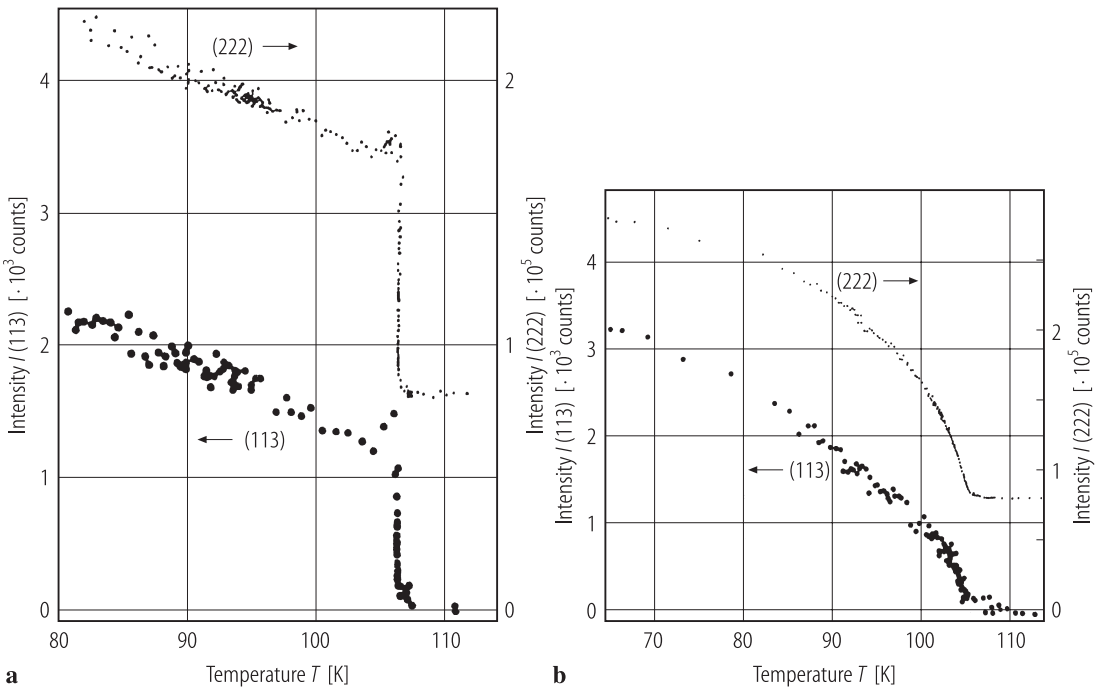

Fig. 1A-8-164. $SrTiO_3$. *I* vs. *T* [83Oka]. *I*: reflection intensity ((222), (113)). (**a**) Temperature was slowly increased and kept at Θ_{II-I} (≈106 K) for 10 h. *I* (113) below Θ_{II-I} includes $\lambda/2$ contribution. (**b**) Temperature was continuously lowered through Θ_{II-I}.

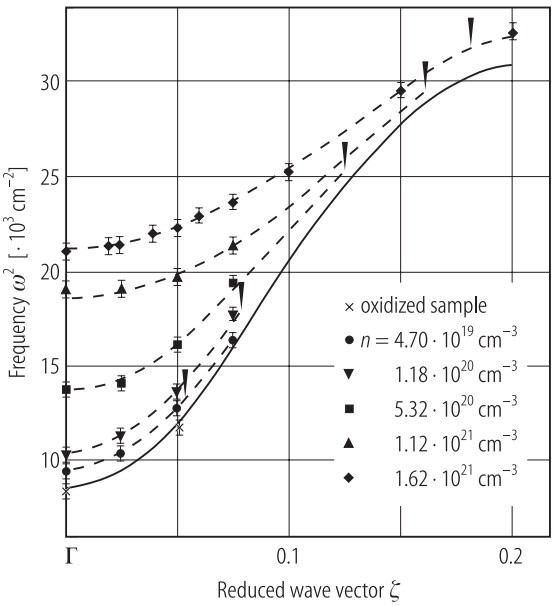

Fig. 1A-8-165. $SrTiO_3$ (reduced). ω^2 vs. ζ [80Bau]. Parameter: n. ω^2: squared frequency of soft TO phonon, ζ: reduced wave vector in [111] direction, n: concentration of oxygen vacancies. T = 300 K.